LETTERS
PUBLISHED ONLINE: 19 JANUARY 2014 | DOI: 10.1038/NNANO.2013.301
nature nanotechnology

Radial modulation doping in core–shell nanowires

David C. Dillen, Kyounghwan Kim, En-Shao Liu and Emanuel Tutuc*

Semiconductor nanowires are potential candidates for applications in quantum information processing[1,2], Josephson junctions[3,4] and field-effect transistors[5–8] and provide a unique test bed for low-dimensional physical phenomena[9]. The ability to fabricate nanowire heterostructures with atomically flat, defect-free interfaces enables energy band engineering in both axial[10–12] and radial[13–16] directions. The design of radial, or core–shell, nanowire heterostructures relies on energy band offsets that confine charge carriers into the core region, potentially reducing scattering from charged impurities on the nanowire surface[13–16]. Key to the design of such nanoscale heterostructures is a fundamental understanding of the heterointerface properties, particularly energy band offsets and strain. The charge-transfer and confinement mechanism can be used to achieve modulation doping[17–19] in core–shell structures[20,21]. By selectively doping the shell, which has a larger bandgap, charge carriers are donated and confined in the core, generating a quasi-one-dimensional electron system with higher mobility. Here, we demonstrate radial modulation doping in coherently strained Ge–Si$_x$Ge$_{1-x}$ core–shell nanowires and a technique to directly measure their valence band offset. Radial modulation doping is achieved by incorporating a B-doped layer during epitaxial shell growth. In contrast to previous work showing site-selective doping in Ge–Si core–shell nanowires[13,22], we find both an enhancement in peak hole mobility compared with undoped nanowires and observe a decoupling of electron transport in the core and shell regions. This decoupling stems from the higher carrier mobility in the core than in the shell and allows a direct measurement of the valence band offset for nanowires of various shell compositions.

Our modulation doped Ge–Si$_x$Ge$_{1-x}$ core–shell nanowires were grown using a two-step process. First, Ge nanowire cores were grown using a Au-catalysed vapour–liquid–solid (VLS) mechanism, using GeH$_4$ as precursor. Following the Ge nanowire growth, an epitaxial Si$_x$Ge$_{1-x}$ shell was grown *in situ* by ultrahigh-vacuum (UHV) chemical vapour deposition (CVD) using a combination of SiH$_4$ and GeH$_4$ as precursors (see Methods). Two types of radial nanowire heterostructure were grown and investigated. In the first heterostructure type, the Si$_x$Ge$_{1-x}$ shell was grown undoped. In the second, we combined modulation doping using B as acceptor with the epitaxial Si$_x$Ge$_{1-x}$ shell growth. Specifically, during Si$_x$Ge$_{1-x}$ shell growth, B$_2$H$_6$ (100 ppm in He) was introduced for 6 min at the mid-point of the 60 min shell growth. Figure 1a presents a schematic representation of modulation-doped core–shell nanowire growth.

For both types of heterostructure, undoped or modulation-doped, we grew Ge–Si$_x$Ge$_{1-x}$ core–shell nanowires with different relative Si/Ge content in the shell by tuning the GeH$_4$-to-SiH$_4$ gas flow ratios during shell growth[23]. Table 1 summarizes the shell thickness (t_{sh}) and relative Si content (x), determined by transmission electron microscopy (TEM) and energy dispersive X-ray (EDX) spectroscopy, for all the heterostructures investigated. The TEM micrograph in Fig. 1b demonstrates the single-crystal structure of the modulation-doped Ge–Si$_{0.63}$Ge$_{0.37}$ core–shell nanowire (sample C in Table 1), together with the expected dopant position.

The epitaxial quality of the core–shell interface was further revealed by the Raman spectra of Fig. 1c, which show a shift of the core–shell nanowire's Ge–Ge mode to higher frequencies compared with the bare Ge nanowire mode at 300.5 cm^{-1}. This blueshift is attributed to a compressive strain in the Ge core due to mismatch of the equilibrium lattice constant at the core–shell interface[24,25] and is present along the entire length of the nanowire. A comparison of Raman mode frequencies with lattice dynamical theory calculations combined with a continuum elasticity strain model[24,25] show very good agreement, indicating little or no strain relaxation and a nominally defect-free core–shell interface in our samples.

To probe the electrical characteristics of the nanowire heterostructures, we fabricated Ge–Si$_x$Ge$_{1-x}$ core–shell nanowire field-effect transistors (FETs) with an Ω-shaped gate geometry and gate lengths L_g between 250 and 1,500 nm (see Methods). Low-resistance, ohmic contacts were realized by ion implantation with B (ref. 26), allowing for extraction of the intrinsic transport properties of the nanowire. A scanning electron micrograph example of a completed device is shown in Fig. 2a, together with a schematic of the device structure.

We measured the electrical characteristics of each device at temperatures between 77 K and 300 K by probing both the drain current versus drain voltage (I_d–V_d) at fixed gate bias V_g, and I_d–V_g at fixed V_d. Figure 2b,c shows the I_d–V_d and I_d–V_g characteristics, respectively, of a modulation-doped Ge–Si$_{0.45}$Ge$_{0.55}$ core–shell nanowire (sample B) with channel length $L_g = 1{,}050$ nm and diameter $d = 43$ nm. The positive threshold voltage and increasing I_d with decreasing V_g indicate p-type depletion mode operation in the modulation-doped nanowires. We found that the modulation-doped Ge–Si$_{0.45}$Ge$_{0.55}$ core–shell nanowires have a peak mobility μ of 700–1,800 cm^2 V^{-1} s^{-1} at 77 K (see Methods), whereas the non-modulation-doped nanowires with similar shell content show a peak μ of 100–280 cm^2 V^{-1} s^{-1} at 77 K. The increase in mobility thanks to the modulation doping is similar to the mobility enhancement observed in planar, group IV-based modulation-doped field-effect transistors (MODFETs)[27].

Figure 3a presents a comparison of the conductivity G measured at 77 K as a function of V_g in two Ge–Si$_{0.45}$Ge$_{0.55}$ core–shell nanowires, one nominally undoped and one modulation-doped. Figure 3a reveals two findings. First, the threshold voltage of the modulation-doped nanowire is shifted to a more positive value, consistent with p-type doping. More importantly, the G–V_g data show a clear slope change at $V_g = 0.81$ V, corresponding to a gate overdrive of $|V_g - V_{th}| = 0.44$ V. This peculiar feature is consistently present in the modulation-doped Ge–Si$_x$Ge$_{1-x}$ nanowires investigated in our study. In contrast, undoped Ge–Si$_x$Ge$_{1-x}$ core–shell nanowires show an almost linear G–V_g dependence, without noticeable features, a finding also consistent with previous reports[8,16].

To further illuminate the source of the kink in Fig. 3a, we performed finite-element calculations of the hole density p versus V_g, and I_d–V_g for modulation-doped Ge–Si$_x$Ge$_{1-x}$ core–shell nanowires

Microelectronics Research Center, The University of Texas at Austin, 10100 Burnet Road, Austin, Texas 78758, USA. *e-mail: etutuc@mer.utexas.edu

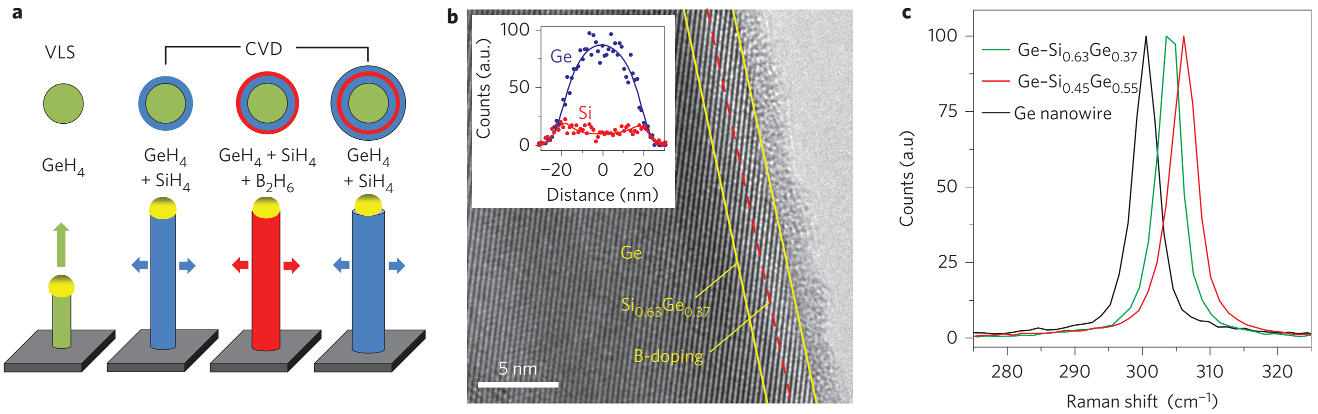

Figure 1 | Nanowire growth and structural characterization. a, Growth schematic for modulation-doped Ge-Si_xGe_{1-x} core-shell nanowires showing the VLS Ge core growth (green) and CVD Si_xGe_{1-x} shell growth (blue) with B modulation-doped region (red). Arrows indicate the growth direction in each regime. **b**, TEM image and EDX linescan data (inset) from a Ge-$Si_{0.63}Ge_{0.37}$ core-shell nanowire. Yellow lines delineate the shell region, and the red dashed line marks the expected position of B dopants. EDX data fitting indicates a $Si_{0.63}Ge_{0.37}$ shell thickness of 3.0 nm. **c**, Raman spectra showing the core Ge-Ge mode from a Ge nanowire (black), and Ge-$Si_{0.45}Ge_{0.55}$ (red) and Ge-$Si_{0.63}Ge_{0.37}$ (green) core-shell nanowires, each of 50 nm diameter. The blueshift of the core-shell spectra indicates a compressively strained core.

Table 1 | Core-shell nanowire growth parameters and measured shell thickness/composition.

Sample	Modulation doping	GeH_4/SiH_4 flow during shell growth (s.c.c.m.)	Shell material	Shell thickness (nm)
A	No	10/50	$Si_{0.46}Ge_{0.54}$	5.2
B	Yes	10/50	$Si_{0.45}Ge_{0.55}$	5.0
C	Yes	5/50	$Si_{0.63}Ge_{0.37}$	3.0

See Methods for further details about the growth process.

(see Methods). Figure 3b shows p versus V_g in both the core and shell regions. At large positive V_g, both the core and shell are fully depleted of carriers. As V_g is decreased to 1.1 V, holes begin to populate the core first, thanks to the positive valence band offset, $\Delta E_v = E_{v,Ge} - E_{v,SiGe}$. Further decreasing V_g to negative values will induce holes in the shell, accompanied by saturation of the core's hole density as a function of V_g (Fig. 3b). A radial slice of the valence band energy (black line) and p (red line) under these biasing conditions is shown in Fig. 3c. Hole density calculations were also performed for Ge–Si_xGe_{1-x} core–shell nanowires without modulation doping (Supplementary Fig. 1). These results are qualitatively similar to the Fig. 3b data, except for a negative shift in the voltage required to populate both core and shell regions, together with a slight decrease in the saturation level of the core hole density. The V_g value at the onset of shell hole occupation is evident in the I_d–V_g calculations of Fig. 3d, which show a kink in the slope of the I_d–V_g curve at the same V_g. As we show in Fig. 3d, the kink position (V_{kink}) depends on the core-to-shell band offset and shifts to higher V_g as the defined ΔE_v is decreased.

The combination of experimental data and finite-element calculations strongly suggests that the kink observed in the G–V_g data of modulation-doped Ge–Si_xGe_{1-x} core–shell nanowires marks the onset of the shell being populated with carriers at high gate overdrive and stems from a larger carrier scattering rate in the shell due to fixed charge impurities. At low gate overdrive, the carriers are confined to the Ge core and the ionized acceptor impurity scattering rate is low. By populating the shell, we effectively decrease the hole mobility due to additional ionized impurity scattering, resulting in an abrupt decline of the slope of the I_d–V_g data. In a heterostructure with small ΔE_v, the core hole density saturation and shell population occur at a relatively low gate overdrive, resulting in a small $|V_{th} - V_{kink}|$. As ΔE_v increases, the onset of shell population

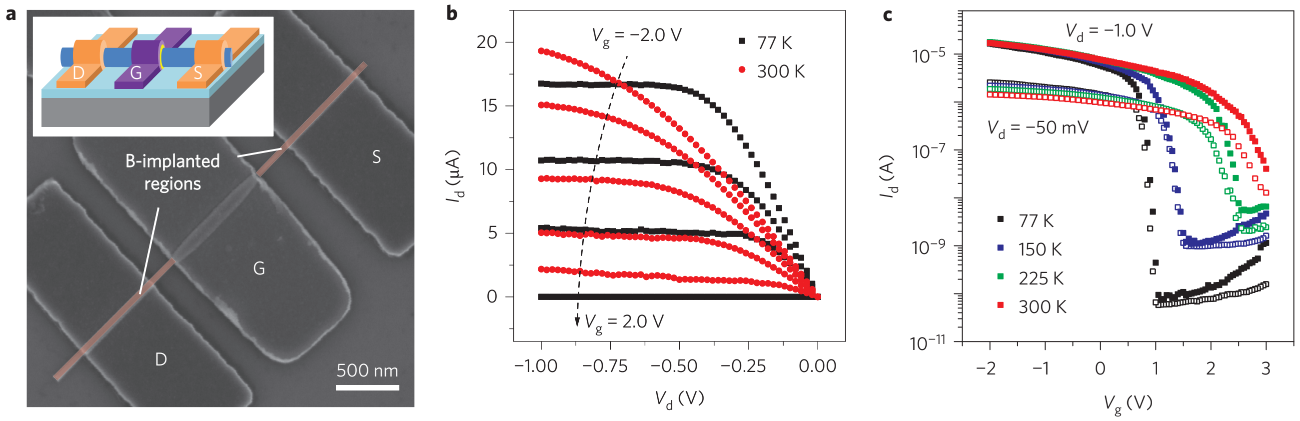

Figure 2 | Modulation-doped core-shell nanowire FETs. a, Scanning electron micrograph of a modulation-doped Ge-$Si_{0.45}Ge_{0.55}$ core-shell nanowire showing B-implanted regions, the gate (G), drain (D) and source (S) contacts, and a schematic of a similar device (inset). **b**, I_d–V_d characteristics of a modulation-doped Ge-$Si_{0.45}Ge_{0.55}$ core-shell nanowire ($d = 43$ nm, $L_g = 1{,}050$ nm) at 77 K and 300 K, taken at $-2.0\ \mathrm{V} < V_g < 2.0$ V, with increments of 1 V. **c**, I_d–V_g characteristics of the same device as in **b**, measured for $V_d = -0.05$ V (open symbols) and $V_d = -1.0$ V (filled symbols) at different temperatures.

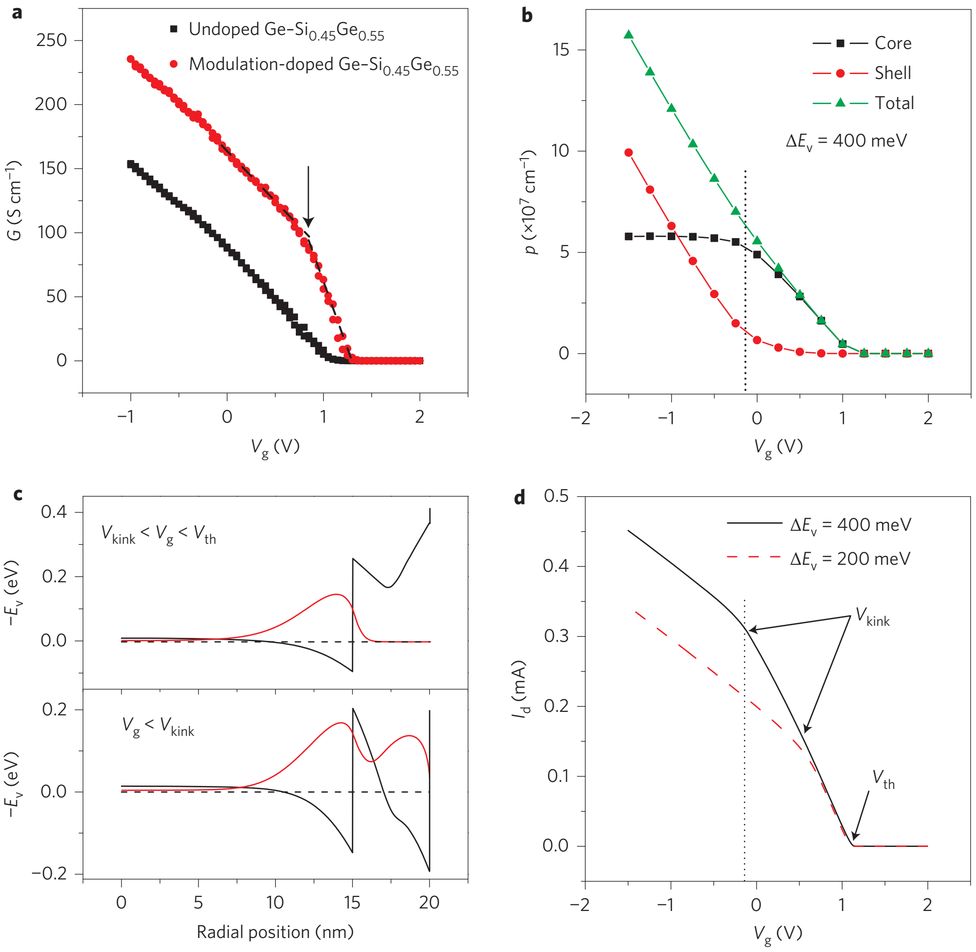

Figure 3 | Decoupled core and shell transport in modulation-doped nanowires. **a**, Comparison of G–V_g experimentally measured for an undoped and a modulation-doped Ge–$Si_{0.45}Ge_{0.55}$ core–shell nanowire at 77 K. A clear kink, marked with an arrow, is observed for the modulation-doped nanowires. The dashed lines are guides to the eye to help identify the kink position. **b**, Core (black), shell (red) and total (green) hole densities per unit length calculated as a function of V_g for the modulation-doped nanowire heterostructure, assuming $\Delta E_v = 400$ meV. The dotted line designates the threshold for hole population of the shell. **c**, Radial dependence of the valence band edge (black) and hole density (red) for the modulation-doped nanowire at two different V_g. Dashed lines indicate the Fermi energy. **d**, Calculated I_d–V_g data for the same heterostructure as in **a**–**c** for two different values of ΔE_v. The dotted line marks the kink in I_d–V_g for $\Delta E_v = 400$ meV.

is at a larger gate overdrive, rendering the $|V_{th}-V_{kink}|$ value an important fingerprint of the modulation-doped heterostructure and a useful tool in quantitatively probing ΔE_v.

The calculations of Fig. 3d were repeated for samples B and C using different ΔE_v values and with shell thickness, Al_2O_3 thickness (t_{ox}) and nanowire diameter values corresponding to experiments. For completeness, we also probed the impact of charge traps at the shell–insulator interface (D_{it}) by simulating structures with $D_{it} = 0$ and 5×10^{12} cm^{-2} eV^{-1}. Figure 4a shows the extracted values of $|V_{th}-V_{kink}|$ for a Ge–$Si_{0.45}Ge_{0.55}$ core–shell nanowire with $t_{sh} = 5.0$ nm, $t_{ox} = 8.35$ nm and $d = 40$ nm. Thanks to the lower effective gate capacitance when traps are considered, there is a stretch-out of the I_d–V_g curve and a corresponding increase in $|V_{th}-V_{kink}|$.

The combination of G–V_g data (Fig. 3a) and finite-element calculations of $|V_{th}-V_{kink}|$ versus ΔE_v (Fig. 4a) provide a powerful method to extract the band offset (ΔE_v) in core–shell nanowires. The extracted ΔE_v values in our samples are shown in Fig. 4b, assuming both $D_{it} = 0$ and 5×10^{12} cm^{-2} eV^{-1}. In the zero trap density case, we find an average ΔE_v of 130 meV over seven devices at $x = 0.45$, increasing to 270 meV (six devices) at $x = 0.63$. If we assume a realistic $D_{it} = 5 \times 10^{12}$ cm^{-2} eV^{-1} value[16], the average of the extracted ΔE_v falls to 100 meV ($x = 0.45$) and 230 meV ($x = 0.63$). The estimated error in ΔE_v data is ±8.5 meV, as determined by the change in calculated $|V_{th}-V_{kink}|$ due to an uncertainty in shell thickness of ±0.5 nm. The scatter in Fig. 4b data stems from sample-to-sample processing variations, such as variations in oxide thickness or dielectric constant, and errors in determining the experimental $|V_{th}-V_{kink}|$ value.

For comparison, in Fig. 4b we plot the ΔE_v values for two different planar Si_xGe_{1-x}–Ge heterostructures. The solid line depicts core-level electron energy loss spectroscopic (EELS) measurements of ΔE_v at an unstrained Si_xGe_{1-x}–Ge interface[28], while the dashed line corresponds to ΔE_v between strained Si_xGe_{1-x} and a cubic Ge substrate, calculated using an empirical pseudopotential method[29]. Although the strain distribution in the core–shell nanowire is expected to be more complicated than that of the planar structure[30–32], our ΔE_v data from modulation-doped Ge–Si_xGe_{1-x} core–shell nanowires match relatively well with calculations for the strained planar structure (dashed line). The unstrained curve (solid line) overestimates our ΔE_v data at all values of x.

Based on these results and those of previous works, high-mobility Ge–Si_xGe_{1-x} core–shell nanowires should have a large Si shell composition (x) to maximize the valence band confinement energy and hole mobility[16], while also reducing the interface trap

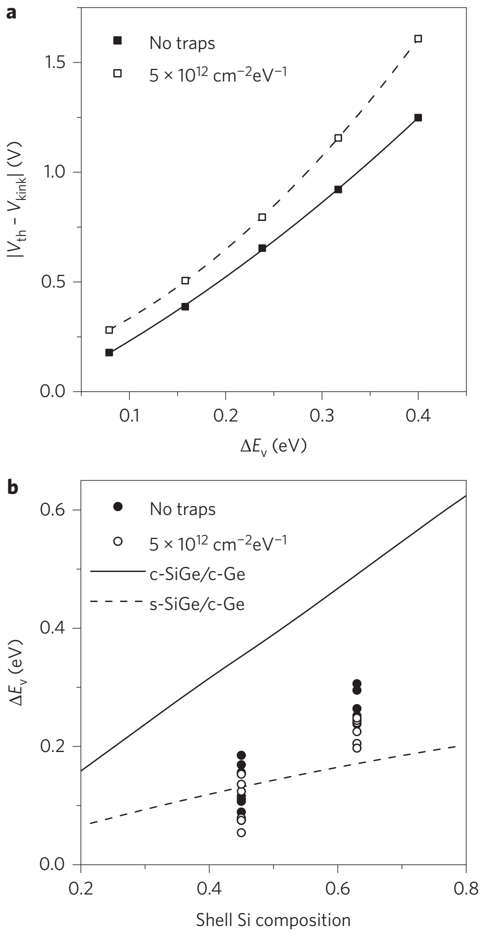

Figure 4 | Valence band offset extraction. a, Calculated $|V_{th}–V_{kink}|$ versus ΔE_v for a 40-nm-diameter modulation-doped Ge-$Si_{0.45}Ge_{0.55}$ core-shell nanowire, with $t_{sh} = 5.0$ nm and Al_2O_3 thickness $t_{ox} = 8.35$ nm. Filled symbols represent calculations with $D_{it} = 0$, and open symbols correspond to $D_{it} = 5 \times 10^{12}$ cm^{-2} eV^{-1}. **b**, ΔE_v extracted from experimental $|V_{th}–V_{kink}|$ values of modulation-doped Ge-Si_xGe_{1-x} core-shell nanowires at 77 K assuming both $D_{it} = 0$ (filled symbols) and $D_{it} = 5 \times 10^{12}$ cm^{-2} eV^{-1} (open symbols). The solid line represents previously measured ΔE_v vales in unstrained planar Ge-Si_xGe_{1-x} interfaces[28], while the dashed lines are calculated ΔE_v values in strained Si_xGe_{1-x} on cubic Ge (ref. 29).

density[33]. At large Si composition, however, the increased lattice mismatch may lead to roughening of the shell surface[31], requiring a balancing of these two competing factors.

In summary, we demonstrate modulation-doping of Ge–Si_xGe_{1-x} core–shell nanowires and observe a decoupling of electron transport between the core and shell regions. The I_d–V_g data in modulation-doped nanowires have a clear kink, marking the onset of the shell being populated with carriers. The measured voltage difference $|V_{th}–V_{kink}|$ is used to extract the core-to-shell valence band offset. We find that ΔE_v is tunable through changes to the shell's material composition.

Methods

Ge–Si_xGe_{1-x} core–shell nanowire growth and structure characterization. A 7-Å-thick Au layer was evaporated onto a Si(111) wafer following removal of native oxide in dilute hydrofluoric (HF) acid. The wafer was then transferred to the cold-wall UHV growth chamber and annealed for 15 min in H_2 ambient at ~370 °C to produce Au nanoparticles, which act as a catalyst for nanowire growth. The Ge nanowire core was grown using the VLS process at a substrate temperature of ~280 °C using GeH_4 (20.8% in He, 50 s.c.c.m.) precursor at 2.5 torr. Because of the finite radial Ge growth rate during VLS core growth, we see a slight tapering of the Ge core diameter from base to tip. The Si_xGe_{1-x} shell was then grown epitaxially *in situ* onto the Ge core using UHV chemical vapour deposition at ~380 °C, with GeH_4 (20.8% in He, 5 or 10 s.c.c.m.) and SiH_4 (100%, 50 s.c.c.m.) precursors, at a total chamber pressure of 40 mtorr. Boron modulation doping was incorporated into the shell growth by the addition of B_2H_6 (100 ppm in He, 50 s.c.c.m.) to the gas ambient. After stopping the B_2H_6 flow, the chamber pressure was briefly lowered to UHV to minimize the thickness of the doped region. Nanowire imaging and EDX shell thickness and composition measurements were carried out using a JEOL 2010F TEM. Raman measurements were taken in a backscattering geometry using a Renishaw inVia spectrometer with a 532 nm incident laser at ~13 kW cm^{-2}. A glass substrate was used to minimize the overlap of the substrate's spectrum with that of the nanowire.

Fabrication of nanowire FETs. Nanowires were removed from the growth substrate by sonication in ethanol, followed by dispersal on a 54 nm SiO_2/n^+ Si(100) substrate, which can also serve as the backgate. We then grew an 8-nm-thick Al_2O_3 top-gate dielectric using atomic layer deposition, which yielded conformal film growth. The top gate was defined using electron-beam lithography, sputtered tantalum nitride (TaN) and lift-off in acetone. The Al_2O_3 film was then etched from the source and drain regions in dilute HF acid. To realize a low extrinsic series resistance in these devices, the samples were B-implanted at an energy of 3 keV and a dose of 1×10^{15} cm^{-2}, using the TaN gate as the implant mask. Dopants were activated in a rapid thermal annealing furnace at 500 °C for 5 min in N_2 ambient. To complete device fabrication, 80-nm-thick Ni source–drain contacts were defined by electron-beam lithography, electron-beam evaporation and lift-off in acetone.

Nanowire mobility extraction. The measured resistance R_m of the nanowire FET is the sum of the intrinsic nanowire channel resistance R_{ch}, the contact resistance R_c and the ungated source–drain extension resistance R_{ext}. The nanowire resistivity and R_c values of 3.0 ± 0.4 mΩ cm and 300 ± 200 Ω, respectively, were determined using data from B-implanted nanowires[26]. The external series resistance ($R_c + R_{ext}$) of the devices probed in this work was 15.8 ± 2.3 kΩ. We determined μ as a function of V_g using $\mu = L_g(R_{ch}ep)^{-1}$, where $R_{ch} = R_m–(R_c + R_{ext})$ and $p(V_g)$ is the hole density per unit length as determined by finite-element calculation.

Finite-element calculations of hole density and transport. The hole density was obtained through a finite-element calculation (Sentaurus, Synopsys) using a full quantum-mechanical solution based on a density gradient model, with the modulation doping density set to 1×10^{20} cm^{-3} over a thickness of 1.0 nm and assuming a temperature of 77 K. A gate-all-around structure was used in place of the actual Ω-shaped gate for computational efficiency, although the results obtained using both structures were identical. For transport calculations, we used a constant mobility model with explicitly defined core and shell values of 1,900 and 450 cm^2 V^{-1} s^{-1}, respectively. These values were chosen only to be comparable to experimental values, not to exactly match experimental I_d–V_g data. It should be noted that the actual mobilities used in simulation are inconsequential, as $|V_{th}–V_{kink}|$, the parameter of interest in this study, was found to be constant over large changes in mobility. We must, however, choose mobilities such that $\mu_{core} > \mu_{shell}$ in order to observe a kink in simulated I_d–V_g curves, a situation activated experimentally with the addition of modulation doping.

Received 17 May 2013; accepted 6 December 2013;

References

1. Hu, Y. *et al.* A Ge/Si heterostructure nanowire-based double quantum dot with integrated charge sensor. *Nature Nanotech.* **2,** 622–625 (2007).
2. Nadj-Perge, S., Frolov, S. M., Bakkers, E. P. A. M. & Kouwenhoven, L. P. Spin–orbit qubit in a semiconductor nanowire. *Nature* **468,** 1084–1087 (2010).
3. Xiang, J., Vidan, A., Tinkham, M., Westervelt, R. M. & Lieber, C. M. Ge/Si nanowire mesoscopic Josephson junctions. *Nature Nanotech.* **1,** 208–213 (2006).
4. Nilsson, H. A., Samuelsson, P., Caroff, P. & Xu, H. Q. Supercurrent and multiple Andreev reflections in an InSb nanowire Josephson junction. *Nano Lett.* **12,** 228–233 (2012).
5. Auth, C. P. & Plummer, J. D. Scaling theory for cylindrical, fully-depleted, surrounding-gate MOSFETs. *IEEE Electron. Dev. Lett.* **18,** 74–76 (1997).
6. Wang, D. *et al.* Germanium nanowire field-effect transistors with SiO_2 and high-κ HfO_2 gate dielectrics. *Appl. Phys. Lett.* **83,** 2432–2434 (2003).
7. Bryllert, T., Wernersson, L-E., Froberg, L. E. & Samuelson, L. Vertical high-mobility wrap-gated InAs nanowire transistor. *IEEE Electron. Dev. Lett.* **27,** 323–325 (2006).
8. Xiang, J. *et al.* Ge/Si nanowire heterostructures as high-performance field-effect transistors. *Nature* **441,** 489–493 (2006).
9. Kloeffel, C., Trif, M. & Loss, D. Strong spin–orbit interaction and helical hole states in Ge/Si nanowires. *Phys. Rev. B* **84,** 195314 (2011).
10. Wu, Y., Fan, R. & Yang, P. Block-by-block growth of single-crystalline Si/SiGe superlattice nanowires. *Nano Lett.* **2,** 83–86 (2002).
11. Björk, M. T. *et al.* Few-electron quantum dots in nanowires. *Nano Lett.* **4,** 1621–1625 (2004).
12. Fuhrer, A. *et al.* Few electron double quantum dots in InAs/InP nanowire heterostructures. *Nano Lett.* **7,** 243–246 (2007).

13. Lauhon, L. J., Gudiksen, M. S., Wang, D. & Lieber, C. M. Epitaxial core–shell and core–multishell nanowire heterostructures. *Nature* **420,** 57–61 (2002).
14. Lu, W., Xiang, J., Timko, B. P., Wu, Y. & Lieber, C. M. One-dimensional hole gas in germanium/silicon nanowire heterostructures. *Proc. Natl Acad. Sci. USA* **102,** 10046–10051 (2005).
15. Jiang, X. *et al.* InAs/InP radial nanowire heterostructures as high electron mobility devices. *Nano Lett.* **7,** 3214–3218 (2007).
16. Nah, J., Dillen, D. C., Varahramyan, K. M., Banerjee, S. K. & Tutuc, E. Role of confinement on carrier transport in Ge–SiGe core–shell nanowires. *Nano Lett.* **12,** 108–112 (2011).
17. Dingle, R., Störmer, H. L., Gossard, A. C. & Wiegmann, W. Electron mobilities in modulation-doped semiconductor heterojunction superlattices. *Appl. Phys. Lett.* **33,** 665–667 (1978).
18. People, R. *et al.* Modulation doping in GeSi/Si strained layer heterostructures. *Appl. Phys. Lett.* **45,** 1231–1233 (1984).
19. Abstreiter, G., Brugger, H., Wolf, T., Jorke, H. & Herzog, H. J. Strain-induced two-dimensional electron gas in selectively doped Si/SiGe superlattices. *Phys. Rev. Lett.* **54,** 2441–2444 (1985).
20. Lee, H. & Choi, H. J. Single-impurity scattering and carrier mobility in doped Ge/Si core–shell nanowires. *Nano Lett.* **10,** 2207–2210 (2010).
21. Amato, M., Ossicini, S. & Rurali, R. Band-offset driven efficiency of the doping of SiGe core–shell nanowires. *Nano Lett.* **11,** 594–598 (2011).
22. Fukata, N. *et al.* Characterization of impurity doping and stress in Si/Ge and Ge/Si core–shell nanowires. *ACS Nano* **6,** 8887–8895 (2012).
23. Varahramyan, K. M., Ferrer, D., Tutuc, E. & Banerjee, S. K. Band engineered epitaxial Ge–SiGe core–shell nanowire heterostructures. *Appl. Phys. Lett.* **95,** 033101 (2009).
24. Menéndez, J., Singh, R. & Drucker, J. Theory of strain effects on the Raman spectrum of Si–Ge core–shell nanowires. *Ann. Phys. (Leipz.)* **523,** 145–156 (2011).
25. Dillen, D. C., Varahramyan, K. M., Corbet, C. M. & Tutuc, E. Raman spectroscopy and strain mapping in individual Ge–SiGe core–shell nanowires. *Phys. Rev. B* **86,** 045311 (2012).
26. Nah, J., Varahramyan, K., Liu, E-S., Banerjee, S. K. & Tutuc, E. Doping of Ge–SiGe core–shell nanowires using low energy ion implantation. *Appl. Phys. Lett.* **93,** 203108 (2008).
27. Schäffler, F. High-mobility Si and Ge structures. *Semicond. Sci. Technol.* **12,** 1515–1549 (1997).
28. Morar, J. F., Batson, P. E. & Tersoff, J. Heterojunction band lineups in Si–Ge alloys using spatially resolved electron-energy-loss spectroscopy. *Phys. Rev. B* **47,** 4107–4110 (1993).
29. Rieger, M. M. & Vogl, P. Electronic-band parameters in strained SiGe alloys on SiGe substrates. *Phys. Rev. B* **48,** 14276–14287 (1993).
30. Liang, Y., Nix, W. D., Griffin, P. B. & Plummer, J. D. Critical thickness enhancement of epitaxial SiGe films grown on small structures. *J. Appl. Phys.* **97,** 043519 (2005).
31. Schmidt, V., McIntyre, P. C. & Gösele, U. Morphological instability of misfit-strained core–shell nanowires. *Phys. Rev. B* **77,** 235302 (2008).
32. Grönqvist, J. *et al.* Strain in semiconductor core–shell nanowires. *J. Appl. Phys.* **106,** 053508 (2009).
33. Bai, W. P., Lu, N. & Kwong, D-L. Si interlayer passivation on germanium MOS capacitors with high-κ dielectric and metal gate. *IEEE Electron. Dev. Lett.* **26,** 378–380 (2005).

Acknowledgements

This work was supported by the National Science Foundation (grants DMR-0846573 and DMR-0819860) and by the Norman Hackerman Advanced Research Program. The authors thank K. Varahramyan for technical discussions and assistance.

Author contributions

D.C.D. performed nanowire sample growth, nanowire device fabrication and characterization, with assistance from K.K. and E-S.L. D.C.D. and E.T. analysed the data and wrote the paper, with input from all authors.

Additional information

Supplementary information is available in the online version of the paper. Reprints and permissions information is available online at www.nature.com/reprints. Correspondence and requests for materials should be addressed to E.T.

Competing financial interests

The authors declare no competing financial interests.